Fluid dynamics of moving fish in a two-dimensional multiparticle collision dynamics model

Reid, Daniel A. P.; Hildenbrandt, H.; Hemelrijk, C. K.; Padding, J.T.

Published in:
Physical Review E

DOI:
10.1103/PhysRevE.85.021901

Publication date:
2012

Fluid dynamics of moving fish in a two-dimensional multiparticle collision dynamics model

Daniel A. P. Reid,[1] H. Hildenbrandt,[1] J. T. Padding,[2] and C. K. Hemelrijk[1,*]

[1]*Behavioural Ecology & Self-organization & Theoretical Biology, Rijksuniversiteit Groningen, Nijenborgh 7, Groningen, The Netherlands*

[2]*Department of Chemical Engineering and Chemistry, Eindhoven University of Technology, P.O. Box 513, NL-5600 MB Eindhoven, The Netherlands*

(Received 19 August 2009; revised manuscript received 20 January 2011; published 2 February 2012)

The fluid dynamics of animal locomotion, such as that of an undulating fish, are of great interest to both biologists and engineers. However, experimentally studying these fluid dynamics is difficult and time consuming. Model studies can be of great help because of their simpler and more detailed analysis. Their insights may guide empirical work. Particularly the recently introduced multiparticle collision dynamics method may be suitable for the study of moving organisms because it is computationally fast, simple to implement, and has a continuous representation of space. As regards the study of hydrodynamics of moving organisms, the method has only been applied at low Reynolds numbers (below 120) for soft, permeable bodies, and static fishlike shapes. In the present paper we use it to study the hydrodynamics of an undulating fish at Reynolds numbers 1100–1500, after confirming its performance for a moving insect wing at Reynolds number 75. We measure (1) drag, thrust, and lift forces, (2) swimming efficiency and spatial structure of the wake, and (3) distribution of forces along the fish body. We confirm the resemblance between the simulated undulating fish and empirical data. In contrast to theoretical predictions, our model shows that for steadily undulating fish, thrust is produced by the rear 2/3 of the body and that the slip ratio U/V (with U the forward swimming speed and V the rearward speed of the body wave) correlates negatively (instead of positively) with the actual Froude efficiency of swimming. Besides, we show that the common practice of modeling individuals while constraining their sideways acceleration causes them to resemble unconstrained fish with a higher tailbeat frequency.

DOI: 10.1103/PhysRevE.85.021901 PACS number(s): 87.10.−e, 47.63.M−

I. INTRODUCTION

The swimming of fish is a topic of broad interest [1], not only to biologists [2–6] but also to engineers [7,8]. In this context, undulatory swimming is important because it is an efficient mode of locomotion, both when swimming alone [7] and in groups [9]. However, it is still unknown what influences the efficiency of undulatory swimming. It has been difficult, both empirically and theoretically, to accurately determine this [10]. For example, a number of theoretical predictions has not yet been tested, such as (1) that thrust is produced by the kinematics of only the tailtip, and (2) that the swimming efficiency is indicated by the slip ratio U/V between the forward swimming speed U and the rearward speed of the body wave V. Also untested is the simplifying assumption of many computational models that fish despite being constrained in their acceleration still swim naturally [11–16]. To test these questions empirically is difficult. Therefore, in the present paper we use a computer model (the so-called multiparticle collision dynamics method) to do so, because of its accuracy in all aspects of hydrodynamics [17] and its suitability to model biological hydrodynamics [18].

Models are needed because of the empirical difficulties of studying the kinematics and hydrodynamics of swimming fish. Empirical measurements of the hydrodynamics are hardly possible yet, and all empirical studies of swimming fish are labor intensive: They involve filming the fish and frame-by-frame analysis of swimming kinematics [19] and flows (using particle-seeded water) [20–24]. Further, the calculation of Froude efficiency is based on the forces of thrust and drag, which for a steadily swimming fish cancel each other out. To determine these forces accurately, according to Dabiri [25] not only the velocity field but also the pressure field around the fish should be measured. This is however not possible so far empirically, but can easily be done in models.

Both mathematical and computational models have been used to study the hydrodynamics of swimming fish. The mathematical models greatly simplify both the fish and the fluid: The fish are represented by rods, flat plates, or airfoils, and the fluid is represented without viscosity [11,26–30]. Due to these simplifications, even the most influential mathematical theory (the elongated body theory [31]) is inaccurate, specifically as regards its use of the slip ratio U/V to indicate swimming efficiency [7,15,16,32,33].

Recent increases in computational power have made it possible to use computer models that take into account both viscosity and the detailed shape of fish. These computational models can be divided in two classes, namely numerical methods and particle-based ones.

Earlier numerical methods simulate hydrodynamics of swimming by approximating the Navier-Stokes equations on a spatial grid. In these models, however, the calculations of the interactions between the fluid and the organism are complex [15,16,34,35], whether the grid is continually adapted to the shape of the fish as in the older models [7,10,12,36] or is kept fixed, as in newer models, e.g., the immersed boundary method [37].

The particle-based methods simulate hydrodynamics through particles that move and collide. From these interactions at the microscale, hydrodynamics according to the Navier-Stokes equations emerge at the macroscale. The particles may be restricted to a grid, such as in the commonly used lattice Boltzmann method [14], or move freely, as in

*c.k.hemelrijk@rug.nl

several other methods [17,38,39]. For the case in which they move freely, the interactions among particles may be smoothed over longer ranges, such as in in the smoothed particle hydrodynamics method [38,39], or be more local, as in the multiparticle collision dynamics method [17]. Multiparticle collision dynamics has been shown to produce hydrodynamics consistent with the Navier-Stokes equations [40–42]. It has been used to model biological motion at a microscopic scale (i.e., at Reynolds numbers below 10^{-2}). Examples include groups of swimming sperm cells [43], star polymers under shear flow [44] and tumbling red blood cells [45], and our recent study of stiff fishlike shapes [18].

All theoretical models make predictions and simplifying assumptions. Here we investigate the correctness of two predictions and one common simplification in the multiparticle collision dynamics method. The first two originate from the elongated body theory [11,31,46]. They are, first, the prediction that thrust of swimming fish is produced only by the kinematics of the tailtip and, second, that the slip ratio U/V indicates swimming efficiency [31]. Further, the implicit assumption—used in many computational models—is that fish that are constrained from accelerating still show natural swimming behavior [12–16]. To gain more insight in the effects of constraints, we study fish that are constrained from accelerating forward, sideways, or in both directions.

We choose the multiparticle collision dynamics method because it has several advantages. First, it models viscosity. Second, it is computationally cheap because it is not continually adapting a grid [7,10,12,15,16,34,36]. Third, due to its lack of a grid it is suitable to study complex, moving shapes. Fourth, it is well suited to parallelization because there are no long-range interactions among the particles [38,39]). This means it can be efficiently executed on a modern graphics card.

Computational efficiency is also the reason that we choose to simulate in two dimensions. Besides the obvious gains due to eliminating one dimension of space, the computational efficiency of two-dimensional simulations is also increased because all flow phenomena occur at lower Reynolds numbers than in three-dimensional simulations [18]. Remarkably, results of two-dimensional models of swimming fish resemble those of real fish remarkably [10,14,47,48].

We validate our model against empirical and theoretical data of thrust and drag of a flapping model of an insect wing [49] and against empirical data of mullets as regards equilibrium swimming speed and the structure and energy of the wake [21].

We study undulating fish over a range of tailbeat frequencies, when they are constrained in their acceleration, forward, sideways, or both. We measure their forward and sideways forces, their slip ratio U/V, their Froude efficiency, and the distribution of forces along the body.

II. METHODS

A. Multiparticle collision dynamics

The model consists of two rectangular environments filled with fluid, one in which an insect wing flaps and another in which a fish undulates. The environment is two-dimensional, homogeneous, contains N identical particles of mass m, and has height H and width W for the insect wing and width W and length L_{box} for the fish (Fig. 1). The positions $\mathbf{x}_i$ and velocities $\mathbf{v}_i$ of the particles are given by two-dimensional vectors of continuous variables. Every time step Δt the particles first move and then collide with each other. Moving leads to new positions $\mathbf{x}_i$ according to the motion equation $\mathbf{x}_i(t+\Delta t) = \mathbf{x}_i(t) + \mathbf{v}_i(t)\Delta t$.

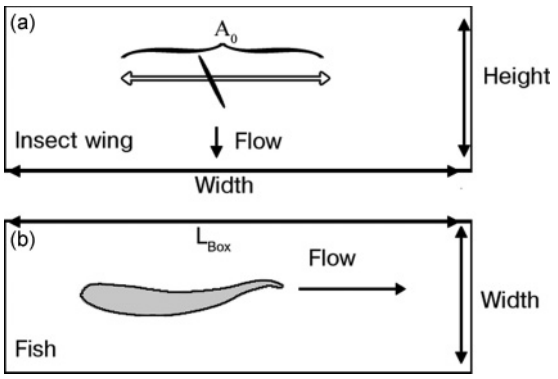

FIG. 1. Overview of the system for (a) the flapping insect wing and (b) the swimming fish. The wing moves along the open arrow, over the distance A_0. The height H and width W of the box (insect wing) and the width W and length L_{box} of the box (fish) are not to scale.

To efficiently simulate collisions between particles, both time and space are coarse-grained by using a square lattice: During the collision step, space is partitioned *temporarily* into cells of size a_0. All particles that are in a particular cell during the collision step are considered to have collided with each other at some moment in the preceding movement step, during which the particles moved in continuous space. To simulate collision, in each lattice cell all particles change their velocities according to $\mathbf{v}_i = \overline{\mathbf{v}} + \Omega \cdot (\mathbf{v}_i - \overline{\mathbf{v}})$. Here $\overline{\mathbf{v}}$ is the mean velocity of the particles in the grid cell and Ω is a stochastic rotation matrix that rotates the velocities by either $+\alpha$ or $-\alpha$ (where α is a fixed system parameter), with equal probability. The rotation direction at a specific moment in time is the same for all particles within a cell but it may differ between time steps. To ensure Galilean invariance we use the method of Ihle and Kroll [50] and displace the lattice every time step by a vector with x and y components which are randomly selected from the uniform interval $[0,a_0)$.

An advantage of the multiparticle collision dynamics method is that several transport properties, such as the shear viscosity and the viscous friction, have been analytically calculated for it [41]. The most important one for this study is the dynamic viscosity μ, which consists of two components:

$$\mu = \mu_{\text{kin}} + \mu_{\text{coll}}, \tag{1}$$

where μ_{kin} is the kinetic component of the viscosity (momentum transported through motion of the particles) and μ_{coll} is the collisional component (momentum transported through interactions between the particles). The equations for the components of the viscosity for the 2D model are [41]

$$\mu_{\text{kin}} = \frac{\rho k_B T \Delta t}{a_0^2}\left[\frac{\rho}{(\rho - 1 + e^{-\rho})(1-\cos 2\alpha)} - \frac{1}{2}\right], \tag{2}$$

TABLE I. Parameter values used. All values are in simulation units.

Parameter name	Symbol	Value
Temperature	k_BT	1.0
Lattice cell size	a_0	1.0
Collision rotation angle	α	$\frac{\pi}{2}$
Particle mass	m	1.0
Particles per cell (average)	ρ	8
Time step length	Δt	1.0
Boundary width	B	30
Boundary displacement steepness	n	3
Dynamic viscosity	μ	1.15
Insect wing motion		
Amplitude	A_0	165.0
Chord length	c	58.0
Frequency	f	4×10^{-4}
Amplitude of rotation	β	$\frac{\pi}{4}$
Fish undulation		
Length	L	900.0
Number of edges	N_E	1024
Wave number	k_L	1.8
Tailbeat frequency	f	$4.8–6.3 \times 10^{-4}$

$$\mu_{\text{coll}} = \frac{m(1-\cos\alpha)}{12a_0\Delta t}(\rho - 1 + e^{-\rho}), \tag{3}$$

where ρ is the average number of particles per cell, k_BT is the system temperature, and Δt is the size of the simulation time step (Table I).

B. System boundaries

The studies we use for comparison assume that the flapping cross-section of a plexiglass model of an insect wing [49] and the undulating fish [21] are moving in a homogeneous, infinite field. We adapt our boundary conditions in order to mimic this. To fulfill the criterion of infinite field size, the ordinary periodic boundary conditions suffice. In order to ensure homogeneity of the flow and eliminate irregularities such as vortices, we added a scrambling boundary zone inside the simulation borders (zone B in Fig. 2). The scrambling eliminates local inhomogeneities of both density and velocity by changing both the position and speed of particles: Each particle in the boundary zone has a chance p_{displace} to randomly move to a new position and have its speed overwritten with a new random one drawn from a Maxwell-Boltzmann distribution with mean 0 and temperature k_BT. The probability of displacement smoothly increases from 0 at the inner boundary of the zone to 1 at the outer boundary, following

$$p_{\text{displace}} = \left(1 - \frac{D_{\text{out}}}{B}\right)^n, \tag{4}$$

where D_{out} is the distance to the nearest outer boundary and n determines the steepness of the increase of p_{displace} (Fig. 2). Displacement is parallel to the nearest system edge: If the particle is close to a vertical border its y coordinate is randomized; if it is close to a horizontal border its x coordinate is changed. The zones of vertical and horizontal shuffling connect diagonally in the corners of the simulation. The new coordinate is uniformly distributed over an interval R which lies between these diagonals (Fig. 2).

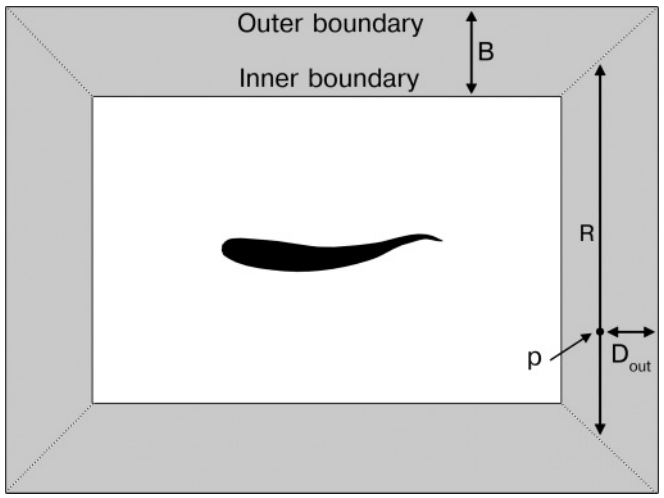

FIG. 2. Scrambling boundary condition. Within the boundary zone of thickness B (not to scale), a particle p's probability to be randomly displaced depends on its distance *Dist* to the outer system edge. Displacement is parallel to the nearest system edge. Dotted lines indicate the boundaries between horizontal and vertical shuffling zones. The new position is along the interval R which lies between these boundaries at distance *Dist* from the outer system edge.

C. Boundary conditions and box size

Our boundary conditions appear to eliminate the vorticity of the flow of both the insect wing [Fig. 3(a)] and the fish [Fig. 3(b)]. However, if the simulation box is too small interactions between the moving organism and the boundary zone may influence our results. To determine the optimal box size, we tested different box sizes for both insect wing and fish. For the insect wing we measured drag and lift and found that the box height must be above 8 chord lengths c to avoid influencing the drag [Fig. 4(a)] but does not influence the lift, and that there were no constraints on width as regards either drag or lift. To be sure to avoid unwanted effects of the edges of the box, we used relatively large boxes of 10×10 chord lengths.

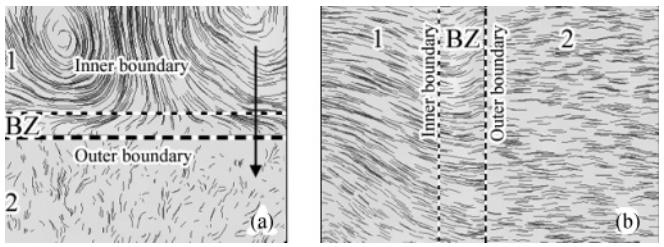

FIG. 3. Elimination of vorticity by the boundary zone for (a) wake of the flapping insect wing and (b) wake of the swimming fish (Fig. 2). The arrow shows overall flow direction. Black lines are truncated streamlines. Localized flow phenomena are eliminated by the boundary zone (BZ) as fluid travels through it from one part of the simulation (1) to another (2).

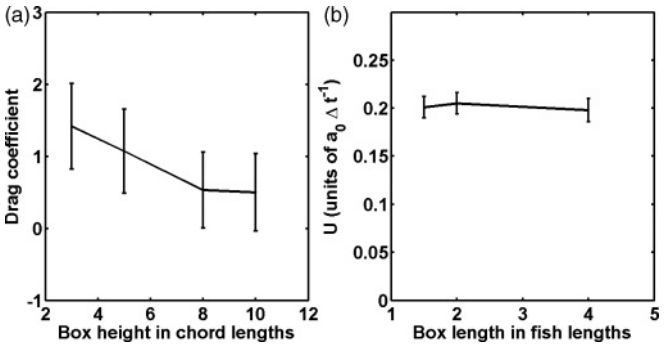

FIG. 4. Effects of size of simulation box on (a) drag coefficient of the cross-section of an insect wing (box size in chord length c of the wing) and (b) equilibrium swimming speed (in simulation units) of the undulating fish (box size in fish body length L).

For the undulating fish, we tested the effect of box size on the equilibrium swimming speed. The box length appeared not to affect the speed [Fig. 4(b)]; thus we conclude that the boundary conditions correctly eliminate momentum and vorticity. For box width, it appeared that for widths below 1 fish length L the swimming speed of the fish increased, due to the channeling effect [9] (data available on request). In order to avoid this and leave space for the wake to develop we use a box length of four body lengths and a box width of one body length.

D. Particle-object collisions

The fluid and organism interact during both the collision and the streaming step. These interactions exchange momentum between the fluid and organism, and ensure that there is no slip at the interface. This is done by two methods, i.e., the fake particle rule during the collision step [51], and the random-reflect rule during the streaming step [42,52]. The fake particle rule is applied to cells which are partially filled by the organism and partially by the fluid. Here we represent the organism by including fake particles in such a number that the number of particles in the cell equals the mean density ρ [Fig. 5(a)]. The velocities of these fake particles are drawn from a Maxwell-Boltzmann distribution with temperature $k_B T$

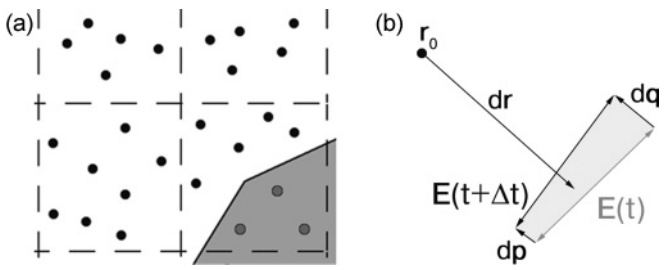

FIG. 5. (a) "Fake particle" boundary condition. Fake particles (indicated in gray) are included in cells which partially overlap the object (indicated in light gray), and where the number of particles is below the mean fluid density. Mean fluid density ρ is 8 (Table I). (b) Schematic overview of the intersection between the path of a moving particle $\mathbf{r}$ and a moving edge $\mathbf{E}$. The precise intersection point depends on the movement speed of both the particle ($d\mathbf{r}$) and of the edge ($d\mathbf{p}$ and $d\mathbf{q}$ for the end points of the edge). The area through which the edge E moves during the time step Δt is indicated in gray.

and a mean velocity which is equal to the local velocity of the organism. Note that the change in momentum due to the rotation of the fake particles is important to include in the hydrodynamical forces on the organism. In case of the fish, omission of this force greatly reduces forward motion (see Fig. S1 in the Supplementary Material [60]).

In the random-reflect boundary condition, particles that hit the organism get a new randomly chosen velocity. The new velocity, relative to the surface, consists of a tangential component v_t and normal component v_n, drawn from the following distributions [42,52]:

$$P(v_t) \propto e^{-\beta v_t^2}, \tag{5}$$

$$P(v_n) \propto v_n e^{-\beta v_n^2}, \tag{6}$$

with $\beta = \frac{m}{2k_B T}$. Both methods also have the benefit that they make the organism act as a weak thermostat because they introduce random velocities of the average system temperature $k_B T$.

The organisms in our models are represented as polygons. This means that their outline is composed of a finite series of lines, so-called edges, which meet at points called vertices. Every time step Δt the vertices move according to the specified motion of the object, which represent the flapping of the wing or the undulation of the fish Eqs. (8) and (10). We use Euler integration, meaning that during a time step the displacement of the vertices is equal to their velocity. The local velocity of any point on the object's surface can be calculated by interpolating the velocities of the two adjacent vertices.

Because the same particle may collide with an object multiple times within one time step Δt, we use the following iterative procedure to determine its trajectory. For each particle, the time δt it has spent moving during the current time step is set to 0. Then, as long as δt is smaller than the length of a time step Δt (Table I), the particle keeps moving. Its movement path is calculated from its velocity vector $\mathbf{v}_i$ as follows: $\mathbf{v}_i \cdot (\Delta t - \delta t)$. If this line intersects one of the edges of an object, a collision occurs at the collision point $\mathbf{x}_{\text{coll}}$ and δt is increased by the amount of time it took to move there. The movement path of a particle can be parametrically expressed as a line segment $\mathbf{r}(t) = \mathbf{r}_0 + t d\mathbf{r}$ with $t \epsilon [0,1]$, where $\mathbf{r}_0$ is its initial position and $d\mathbf{r}$ is its velocity. The motion of the edges of the object is defined by the motion of the vertices at their end points. The movement path of the two vertices connected by an edge can also be expressed as two line segments: Let $\mathbf{p}(t)$ and $\mathbf{q}(t)$ be the position of the vertices over time, as follows: $\mathbf{p}(t) = \mathbf{p}_0 + t d\mathbf{p}$ and $\mathbf{q}(t) = \mathbf{q}_0 + t d\mathbf{q}$. We then also define the edge itself as a line segment, pointing from $\mathbf{p}(t)$ to $\mathbf{q}(t)$. Its starting position is $\mathbf{p}(t)$ and its direction $\mathbf{u}(t)$ is $\mathbf{u}(t) = \mathbf{q}(t) - \mathbf{p}(t)$, or more explicitly,

$$\mathbf{u}(t) = (\mathbf{q}_0 - \mathbf{p}_0) + t\,(d\mathbf{q} - d\mathbf{p})\,. \tag{7}$$

Any point on the edge can be expressed as $\mathbf{E}(s,t) = \mathbf{p}(t) + s\mathbf{u}(t) = s\mathbf{q}(t) + (1-s)\mathbf{p}(t)$.

The movements of particle and edge intersect [Fig. 5(b)] if at any time t' the equality $\mathbf{E}(s,t') = \mathbf{r}(t')$ holds. This gives two equations (one for each component x and y) with two unknowns (s and t'). Solving this leads to a quadratic equation, the roots of which can be found using the quadratic formula. More details can be found in the Appendix.

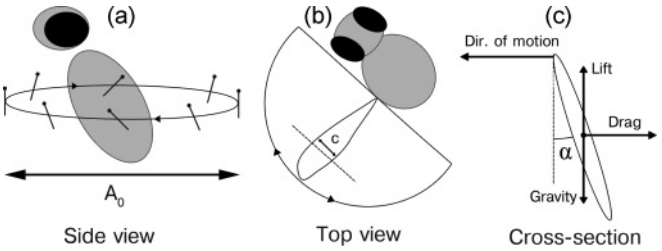

FIG. 6. Schematic overview of a hovering fruit fly. (a) Side view: A series of snapshots of the moving cross-section of the wing as it moves back and forth over distance A_0. The leading edge of the wing is represented by a dot. Movement and rotation of the wing are in phase. The elliptical path of motion is a visual aid: In the simulations the wing does not displace vertically. (b) Top view of the insect: The dashed line shows which cross-section (of chord length c) of the wing we simulate. (c) Forces on the moving wing. The forces act on the center of gravity.

After the collision, the particle gets a new random velocity following Eqs. (5) and (6), with the local speed of the object surface added to the result. If δt is smaller than Δt, it keeps moving, starting from the point of collision $\mathbf{x}_{\text{coll}}$, and may collide several additional times in the same manner.

The force which the fluid exerts on the object during a time step Δt is the opposite of the sum of the change in momenta of all particles that collide with it during that time step, divided by the time step Δt. Note that particles may collide with the body both during the streaming step (as described above) and during the rotation step (through the fake particle rule).

E. Insect wing

Our simulations of the cross-section of an insect wing [Figs. 6(a) and 6(b)], based on those by Wang *et al.* [49], concern a two-dimensional representation of a transverse cross-section of a horizontally beating upscaled model of a wing of a fruit fly (*Drosophila melanogaster*) as it hovers in place. We represent the cross-section of the wing by an ellipse with a thickness ratio of 0.125 [Fig. 6(c)]. We make the wing (with chord length c) move, without it being influenced by the flow around it, as follows. It moves back and forth through the horizontal plane over a distance A_0 while it rotates around its center of mass [Figs. 1(a) and 6(a)]. The position $x(t)$ of the center of the wing cross-section and the angle $\alpha_w(t)$ between the wing and the y axis change over time with frequency f according to

$$x(t) = \frac{A_0}{2}\cos(2\pi f t), \tag{8}$$

$$\alpha_w(t) = \alpha_{w,0} + \beta\sin(2\pi f t + \phi). \tag{9}$$

Here A_0 is the amplitude of the path of the wing, $\alpha_{w,0}$ is the initial angle, β is the amplitude of the angle, and ϕ is the phase difference between the functions of position and angle. This phase difference determines the angle of the wing when it reverses its movement. If there is no phase difference the wing is vertical when its movement reverses, and the wing stroke is symmetrical. If rotation is advanced, the wing is already rotating back from the vertical position before it reaches the extremes of its movement path. If rotation is delayed, the wing has not finished rotating through the vertical as it reaches the extreme of its stroke [49,53]. As in the study of Wang *et al.* [49] we compare the effects on drag and lift of symmetrical ($\phi = 0$), advanced ($\phi = \frac{\pi}{4}$), and delayed ($\phi = \frac{-\pi}{4}$) rotation. We measure the force which the fluid exerts on the moving wing and decompose it into lift and drag components. The insect is hovering; therefore its lift compensates for the gravity. The drag is horizontal and counteracts the wing's motion.

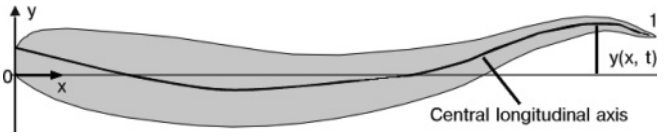

FIG. 7. Schematic overview of the deviation from the central axis of the spine of an undulating mullet.

F. Fish

We study the mullet (*Chelon labrosus*) because it swims at a steady speed by undulating its body without using its pectoral fins [1]. We simulate an undulating horizontal cross-section of a mullet, traced from the body contours presented by Müller *et al.* [21]. Because the shape of the fish is more curved at the head than at the tail, we made the polygonal edges at the head of the fish shorter than those of the rear. Note that the undulation of our simulated fish is not influenced by the flow around it. We formulate the characteristics of the propulsive wave along the body of the fish in terms of the lateral movement of its central, longitudinal axis, or spine [54]. To do so, we consider the spine of the straight fish to have an y value of 0 (Fig. 7). We scale the fish in terms of fractions of its body length L, so that $x = 0$ at the front of the fish and $x = 1$ at its rear. For each point x along the spine of the fish, its lateral deviation from the central axis over time is given by

$$y(x,t) = \theta(x)\sin(k_L x - \omega t). \tag{10}$$

Here $\theta(x)$ is the amplitude envelope function, which varies nonlinearly along the fish body, $k_L = \frac{2\pi}{\lambda}$ is the wave number, which indicates the number of complete sine waves on the body for a wavelength λ, and $\omega = 2\pi f$ is the angular velocity for the tailbeat frequency f. For undulating mullets the amplitude of the wave is smallest behind the head and increases quadratically toward the tail:

$$\theta(x) = \theta_0 + \theta_1 x + \theta_2 x^2. \tag{11}$$

Steady swimming by undulating the body is characterized by two parameters, the Reynolds number Re and the Strouhal number St, which are defined as [1,55]

$$\text{Re} = \frac{\rho U L}{\mu}, \tag{12}$$

$$\text{St} = \frac{A f}{V}, \tag{13}$$

where ρ and μ are respectively the density and dynamic viscosity of the fluid, and the remaining parameters describe the fish: L is its length, U is its swimming speed, f is the frequency of its tailbeat, and A is two times the maximum lateral excursion of its tailtip over the tailbeat cycle, which is used as an approximation of the width of its wake.

To give an individual infinite space in which to swim, we move the simulation box along with it. We do so as follows: Whenever the center of gravity of the fish has moved one cell a_0 away from its original position within the center of the box, we move the box center toward that of the fish by one simulation unit a_0. We shift only when it has moved at least one simulation unit, because smaller shifts may cause floating point rounding errors to accumulate. The shift may be horizontal, vertical, or both. Subsequently, we apply the periodic boundary condition; thus any particles which left the simulation box through one side are reintroduced at the other side of the simulation, with their velocity overwritten with a random one drawn from a Maxwell-Boltzmann distribution with mean 0 and temperature $k_B T$.

To study the effects of constraint on the acceleration of the fish along its two axes of movement (forward and sideways), we test the four possible combinations of constraint: (1) free acceleration along all directions ("unconstrained"), (2) no sideways acceleration ("sideways constrained"), (3) neither forward nor sideways acceleration ("all constrained"), and (4) no acceleration forward ("forward constrained"). If acceleration is unconstrained in at least one direction, we apply along this direction the appropriate component of the net hydrodynamical force to the center of gravity of the fish. So for instance if a fish is sideways constrained, this implies that the center of gravity does not accelerate sideways (Fig. 8). We consider the fish to have a density equal to that of the fluid, and a mass equal to its surface area times the density ρ. To displace the fish, we use Euler integration and change the position of its center of gravity by its speed vector.

To keep the tracking of the forward and sideways direction of the fish as simple as possible, we choose not to apply the torque to rotate the fish. Preliminary tests showed no effect of this omission on the measured variables.

G. Parametrization and experimental setup

In the multiparticle collision dynamics model, objects should not move faster than approximately 20% of the speed of sound in the fluid, because higher speeds cause significant compressibility effects such as shock waves. This means that their Mach number $\mathrm{Ma} = U/U_{\mathrm{sound}}$ should not exceed 1/5 [51,56]. For our parameter settings (Table I), the speed of sound $U_{\mathrm{sound}} = \sqrt{2k_B T/m} = \sqrt{2}$ (see [51]). Thus, the maximum velocity of the organisms in our model per simulation time step is $\frac{1}{5}\sqrt{2} = 0.28a_0/\Delta t$. We conservatively choose a somewhat lower maximum velocity for our default parametrization, $0.2a_0/\Delta t$. This restriction of the velocity limits our choices for the parametrization of the moving organisms.

We parametrize our simulation of the flapping cross section of the wing after the experiments with an upscaled model of a drosophila wing by Wang *et al.* [49]. We tune the Reynolds number (75) to theirs, via the wing chord length c and wing beat amplitude A_0, and the relation $A_0/c = 2.8$ between them. In our simulation the Reynolds number of the insect wing is $\mathrm{Re} = U_{\max} c\rho/\mu = 1.29c$, where the wing's maximum speed $U_{\max}$ is set to 0.2 as previously explained. Thus for a Reynolds number of 75, the chord length $c = 75/1.29 = 58a_0$ and the wing beat amplitude $A_0 = 2.8c = 163a_0$. The experimental insect wing has a chord length of 0.067 m [57]; thus our simulation length scale is $a_0 = 0.067/58 = 0.012$ m.

To determine the size of the simulation time step Δt in seconds, we calculate the ratio between the frequency of the wing beat in our simulation f_{sim} and that of the real wing $f_{\mathrm{real}} = 0.25$ Hz. Because the maximum of the speed function $\frac{\delta}{\delta t}x(t)$ is $U_{\max} = A_0 c\pi f_{\mathrm{sim}}$, we find that for the maximum speed of 0.2 that we chose due to Mach number constraints $f_{\mathrm{sim}} = \frac{0.2}{163\pi} = 3.9 \times 10^{-4}\Delta t^{-1}$. Thus, the simulation time step for the insect wing simulations Δt is 1.6×10^{-3} s (Table II).

Our fish simulations are parametrized to resemble the experimental results of Müller *et al.* [21] as regards undulation envelope, and size (Table II). Our model of a fish is $900a_0$ long, which was the maximum that was computationally feasible on our hardware. Thus our simulation unit of distance $a_0 = \frac{0.126}{900} = 1.4 \times 10^{-4}$ m.

We use the ratio between the swimming speed of the simulated and of the real fish to calculate the length of the simulation time step. The swimming speed is likely to be dependent on the tailbeat frequency [1], which we vary in our simulations. Here we present the time step calculations for the tailbeat frequency of the real mullet; the calculation is the same for other swimming speeds. The swimming speed of the

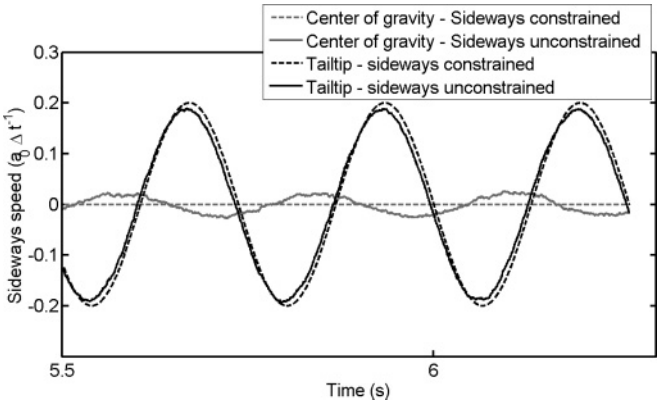

FIG. 8. Sideways speed (in simulation units) over time of the center of gravity of the fish and its tail tip, for fish that either are or are not constrained from sideways acceleration.

TABLE II. Parametrization for the cross section of the insect wing model [49] and the fish in SI units.

Parameter name	Value
Insect wing model	
Amplitude	0.187 m
Chord length	0.067 m
Time step	0.0016 s
Frequency	0.25 s^{-1}
Fish	
Length	0.126 m
Time step	0.00015 s
Tailbeat frequency	3.2–4.2 s^{-1}
Undulation amplitude coefficient θ_0	0.02
Undulation amplitude coefficient θ_1	0.08
Undulation amplitude coefficient θ_2	0.16

model U_{sim} is intended to be $0.2a_0/\Delta t = 1.4 \times 10^{-4}$ m/Δt, and the real fish swims at 0.176 m/s. Therefore $\Delta t = 0.2 \times 1.4 \times 10^{-4}$ s/$0.176 = 1.5 \times 10^{-4}$ s (Table II).

We start the simulations without directional flow, by initializing all particles with random velocities drawn from a Maxwell-Boltzmann distribution of mean 0 and temperature $k_B T$ (Table I). Thus, all directional flow in the simulation is caused by the movement of the organisms. Following the experiments of Wang *et al.* [49] we simulate 4 full wing beats of the insect wing. For the fish we follow the experiments of Müller *et al.* [21] of a fish swimming at steady speed by letting the simulation run until the swimming speed and surrounding flow of the fish reach equilibrium.

H. Computational measurements

For the flapping insect wing, we measure the forces of drag (horizontal) and lift (vertical). Like Wang *et al.* [49], we nondimensionalize these forces by dividing them by the maximal force measured for a steadily moving wing.

For the undulating fish we use the same measurements as the experiments by Müller *et al.* [21]. They estimate the thrust force F_T indirectly, from the circulation Γ of the vortices in the wake. They use this indirect method because the thrust and drag operate along the same axis in opposite directions, and cancel each other out at a constant swimming speed. The circulation Γ of the vortices in the wake is calculated as $\Gamma = \oint_c \mathbf{v} \cdot d\mathbf{l}$, where c is a closed curve around a vortex, $\mathbf{v}$ is the fluid velocity, and $d\mathbf{l}$ is a tangential unit vector along the curve c. From Stokes's theorem, the curve integral can be rewritten as $\Gamma = \mathbf{v}dy' = \int\int \omega dA$, with ω being the vorticity and A the surface area of the vortex. In our method, we therefore sum the vorticity over the area of the vortex.

Due to the stochasticity of the method, spatial averaging is needed to obtain a smooth flow field. We employ a Gaussian convolution with a kernel of $50a_0$.

To measure the stability of the wake of the fish, we study an area of 1.5 body lengths behind the swimming fish. We measure the distances in the direction of swimming between subsequent vortices that rotate in the same direction (dx in Fig. 9), and the distances perpendicular to the swimming direction between subsequent counterrotating vortices (dy in Fig. 9). We establish the center of a vortex by drawing in a screenshot two perpendicular lines through its area of maximal vorticity (the darkest for clockwise or lightest for counterclockwise vortices, respectively), and assuming that the center lies at the intersection point of the two lines. The average distance we calculate over 10 snapshots taken at random intervals. We also measure the forces on the fish directly.

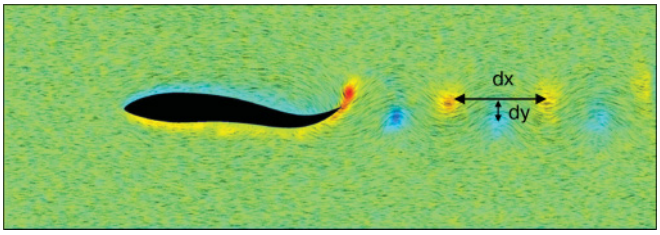

FIG. 9. (Color) Wake of the swimming fish in our model, with truncated streamlines. Distance between vortices in the swimming direction and perpendicular to it are indicated as dx and dy, respectively. Vorticity is shown by the color, with blue indicating clockwise and red indicating counterclockwise vorticity.

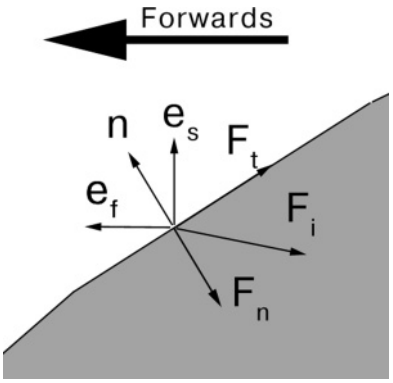

FIG. 10. Decomposition of the force F_i on the skin of the fish into pressure (F_n) and viscous (F_t) components (see Methods). The surface normal is indicated as n and the unit vectors pointing forward and sideways are labeled e_f and e_s.

In our simulations we determine thrust and sideways power as follows. The total forward force F at any moment t is calculated by a summation over the skin edges of the fish (Fig. 10):

$$F(t) = \sum_i \mathbf{F}_i \cdot \mathbf{e}_f = \sum_i \left(\mathbf{F}_n^i \cdot \mathbf{e}_f + \mathbf{F}_t^i \cdot \mathbf{e}_f\right), \qquad (14)$$

where $\mathbf{F}_n^i = (\mathbf{F}_i \cdot \mathbf{n})\,\mathbf{n}$ is the force vector perpendicular to the skin at edge i, $\mathbf{F}_t^i = \mathbf{F}_i - \mathbf{F}_n^i$ is the force vector tangential to the skin, and $\mathbf{e}_f$ is a forward-pointing unit vector. The summations of the first and second element in the last expression thus represent the pressure and viscous contributions, respectively, to the forward force, though it should be noted that if the tangential speed varies strongly around the body the viscous forces may have a small normal component.

To separate the thrust and drag out of this total body force following the method of Borazjani and Sotiropoulos [15], we decompose the force, depending on whether or not the force is positive (thrust) or negative (drag):

$$T(t) = \sum_i \left[\mathbf{F}_n^i \cdot \mathbf{e}_f H\left(\mathbf{F}_n^i \cdot \mathbf{e}_f\right) + \mathbf{F}_t^i \cdot \mathbf{e}_f H\left(\mathbf{F}_t^i \cdot \mathbf{e}_f\right)\right], \qquad (15)$$

$$D(t) = -\sum_i \left[\mathbf{F}_n^i \cdot \mathbf{e}_f H\left(-\mathbf{F}_n^i \cdot \mathbf{e}_f\right) + \mathbf{F}_t^i \cdot \mathbf{e}_f H\left(-\mathbf{F}_t^i \cdot \mathbf{e}_f\right)\right], \qquad (16)$$

where H is the Heaviside step function. Thus, for each edge, for both the perpendicular (pressure) and tangential (viscous) force on it, we add the forward component of the force to the thrust if it is positive, and to the drag if it is negative. The sum of thrust and drag is the total force $F(t)$:

$$F(t) = T(t) - D(t). \qquad (17)$$

We calculate per time step Δt the sideways power P_s which the fish exerts:

$$P_s(t) = \sum_i \mathbf{F}_i \cdot \mathbf{e}_s V_{\text{und}}^i, \qquad (18)$$

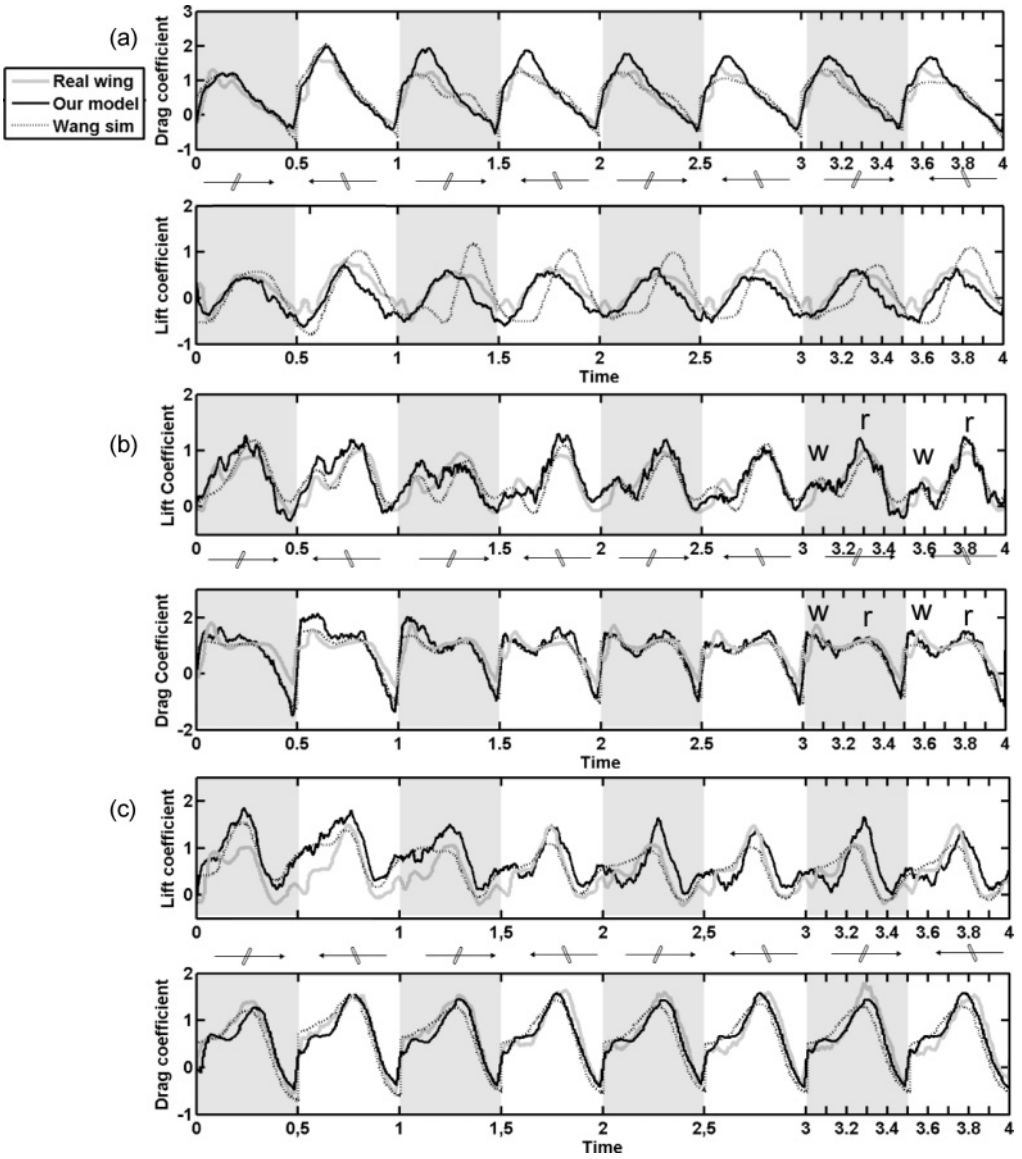

FIG. 11. Drag and lift coefficients of a flapping insect wing over time, at $A_0/c = 2.8$. Light gray areas indicate that the wing moves to the right. Real wing data taken from Wang *et al.* [49]. (a) $\phi = -\frac{\pi}{4}$ (delayed rotation). (b) $\phi = 0$. Force peaks associated with wake capture and rotational forces are labeled "w" and "r", respectively. (c) $\phi = \frac{\pi}{4}$ (advanced rotation).

where $\mathbf{e}_s$ is a unit vector in the sideways direction, and V^i_{und} is the sideways velocity of edge i.

From these forces, we determine the swimming efficiency. Following Tytell and Lauder [23] and Borazjani and Sotiropoulos [15], we use a modified version of the Froude efficiency:

$$\eta = \frac{\bar{T}\bar{U}}{\bar{T}\bar{U} + \bar{P}_s}, \tag{19}$$

where $\bar{T}$ is the mean thrust over a tailbeat cycle, $\bar{U}$ is the mean forward speed of the fish, and $\bar{P}_s$ is the mean sideways power it exerts over a tailbeat cycle. Thus, the Froude efficiency η expresses the percentage of the total power which is converted into forward speed.

To measure the distribution of the forces along the body of the fish, we calculate them for each edge of the polygon that represents the body, and compute the average and standard deviation per segment of the body. Each segment comprises an equal number of edges and thus is shorter near the head.

All programs were implemented in a combination of C++ and OpenGL shading language, and simulations were run on a single Intel Core 2 Quad PC. Single simulations of a 20 tailbeats of a swimming fish took approximately 12 hours on a single PC. Data analysis and visualization were done with MATLAB [58] except for the vorticity plots which were made in our simulations.

III. RESULTS

A. Comparison to empirical data

We verify the correctness of our model on the basis of empirical data of a model of an insect wing [49] and of a swimming mullet [21].

TABLE III. Drag and lift coefficients of the flapping insect wing averaged over time for symmetrical rotation ($\phi = 0$), advanced rotation ($\phi = \frac{\pi}{4}$), and delayed rotation ($\phi = -\frac{\pi}{4}$). Experimental results were time averaged from Figs. 2–4 of Wang *et al.* [49] Expt. are results of their experiments, Sim. are results of our simulations.

	C_L		C_D	
	Expt.	Sim.	Expt.	Sim.
Sym.	0.435	0.477	0.69	0.71
Adv.	0.519	0.656	0.56	0.61
Delay	0.09	0.02	0.529	0.557

For our insect wing, the time series of its drag and lift coefficient resemble the experimental results of Wang *et al.* [49] in all cases: with delayed rotation [Fig. 11(a)], with no phase difference between translation and rotation [Fig. 11(b)], and with advanced rotation [Fig. 11(c)]. Of particular interest is the resemblance regarding two peaks of the drag and lift. One peak occurs close to the moment at which the wing has reversed its direction [Fig. 11(b); indicated with "w" at 3.1 s] while the other happens just after the middle of the wing beat [Fig. 11(b); indicated with "r" at 3.3 s], as the wing is beginning to slow from its maximum velocity and reverses its rotation. The first peak is most likely due to the wing re-encountering its own wake (a phenomenon known as "wake capture" [53]), while the second peak is probably caused by a combination of rotation and deceleration of the wing [49]. We confirm that the wing produces more lift with advanced rotation and much less lift with delayed rotation when compared to a wing with no phase difference (Table III), similar to experimental data [53,59]. Due to the stochastic nature of the method and the small size of the insect wing in terms of grid cells, graphical representations of its flow field were only weakly informative.

Our fish, for the same tailbeat frequency as the real fish, reaches a similar cruising speed (Table IV). Also similarly to real fish, our modeled fish produces a wake with a reverse von Kármán vortex street of alternating, counterrotating vortices, at a fixed distance and angle from each other, with a jet zigzagging between them (Fig. 9; movie in the Supplementary Material [60]). The wake resembles that of a mullet (Fig. 5 in Ref. [21] and Fig. 17) as regards the stability of its structure, the size of the vortex rings R, their angle with the direction of swimming ϕ and their circulation Γ, and the variability of the distances between the vortices (dx and dy in Fig. 9) both in the swimming direction and perpendicular to it (Table IV).

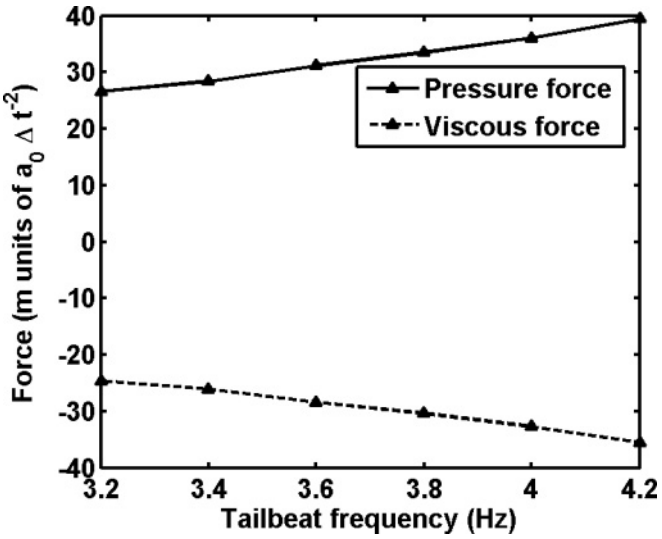

FIG. 12. Force in the swimming direction of the freely swimming fish, decomposed into pressure and viscous component. Positive values indicate thrust, negative drag.

From the correspondence of our results to empirical data [21,49] we conclude that our simulations are sufficiently accurate to further investigate the swimming of fish.

B. Model results

We study the contributions to thrust and drag of forces perpendicular and tangential to the skin. We investigate where on the body thrust and drag are produced, and what the effect is of tailbeat frequency and acceleration-constraints on a number of measures such as swimming speed, thrust, drag, exerted sideways power, slip ratio, Froude efficiency, and Strouhal number.

Thrust appears to be caused mainly by forces perpendicular to the skin (pressure), and drag is caused by tangential forces (viscosity) (Fig. 12). The thrust appears to be produced not only by the tail (segment 8, Fig. 13), but by the complete rear 2/3 of the body (segments 5–8, Figs. 13 and 14). The only area that never produces thrust is the head of the fish, which is responsible for the majority of the drag (segments 1–4, Figs. 13 and 14). The part of the body that produces the least drag is just behind the head of the fish (segment 5, Figs. 13

TABLE IV. Results for the equilibrium swimming speed and wake structure and energy of the swimming fish (Fig. 17). Experimental results are from Müller *et al.* [21]. Experimental vortex spacing estimated from their figures. Error ranges are the standard deviations.

Measure	Simulation value	Experimental value
	Swimming speed	
Equilibrium forward swimming speed U	1.55 L s^{-1}	1.4 L s^{-1}
	Wake structure and energy	
Ring radius R	$104.5a_0 = 1.45$ cm	1.9 cm
Ring angle ϕ	$52^\circ \pm 9^\circ$	$40^\circ \pm 10^\circ$
Circulation Γ	9.6×10^{-4} m^2 s^{-1}	7.6×10^{-4} m^2 s^{-1}
Standard deviation of vortex spacing dx, dy	5%, 5%	6%, 6%

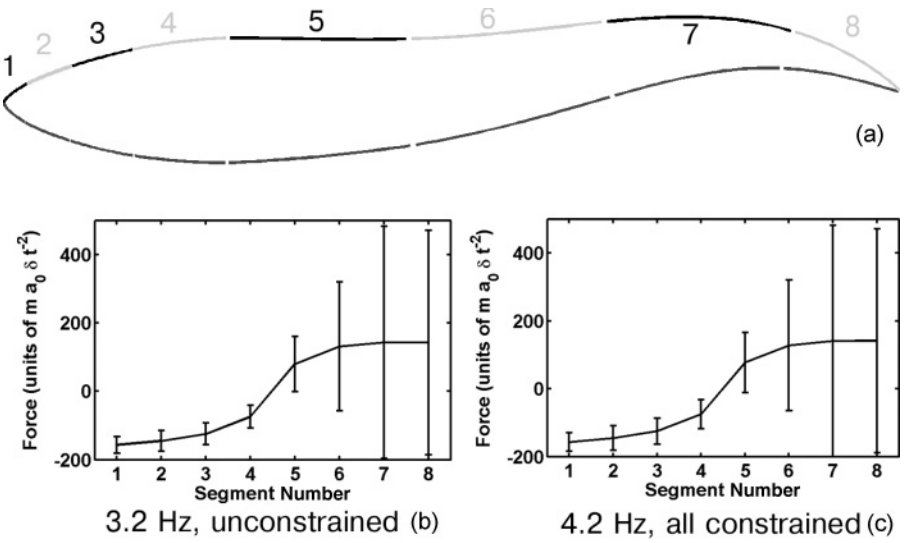

FIG. 13. Force in the swimming direction as distributed over several segments of the skin of the fish, without constraints (a) and with constraint of lateral and forward acceleration (b). Positive values indicate thrust, negative drag. Error bars indicate one standard deviation.

and 14). The locations and strengths of the forces on the skin (Figs. 13 and 14) do not differ across the 6 tailbeat frequencies, 3 acceleration constraints, and the unconstrained fish (data available on request). This similarity is a consequence of the small size of both the time step Δt and of the segments: Differences between different settings can only be detected by averaging over both space and time.

As to the tailbeat frequency in our model, it positively affects forward swimming speed [Fig. 15(a)], average lateral power [Fig. 15(b)], thrust [Fig. 15(c)], and the slip ratio [Fig. 15(d)], and it decreases the Froude efficiency [Eq. (19); Fig. 15(e)]. This arises as follows: With increasing tailbeat frequency, the forward speed increases because of the increased thrust. The Froude efficiency decreases because the sideways power increases more strongly than the forward speed and thrust do. We explain the higher slip ratio (i.e., the higher swimming speed U relative to the rearward speed of the body wave V) as resulting from the increased inertia relative to viscosity (i.e., the increased Reynolds number): When its tailbeat reverses, viscous drag slows the fish down less at higher tailbeat frequency. Thus we also expect the variability of the swimming speed to decrease with the tailbeat frequency. We confirm this by the significant negative correlation between the tailbeat frequency and the coefficient of variation of the swimming speed ($N = 8$, Spearman's $\rho = -0.88$, $p = 0.007$).

The increased tailbeat frequency influences the wake by increasing the radius of the vortex rings and their angle ϕ

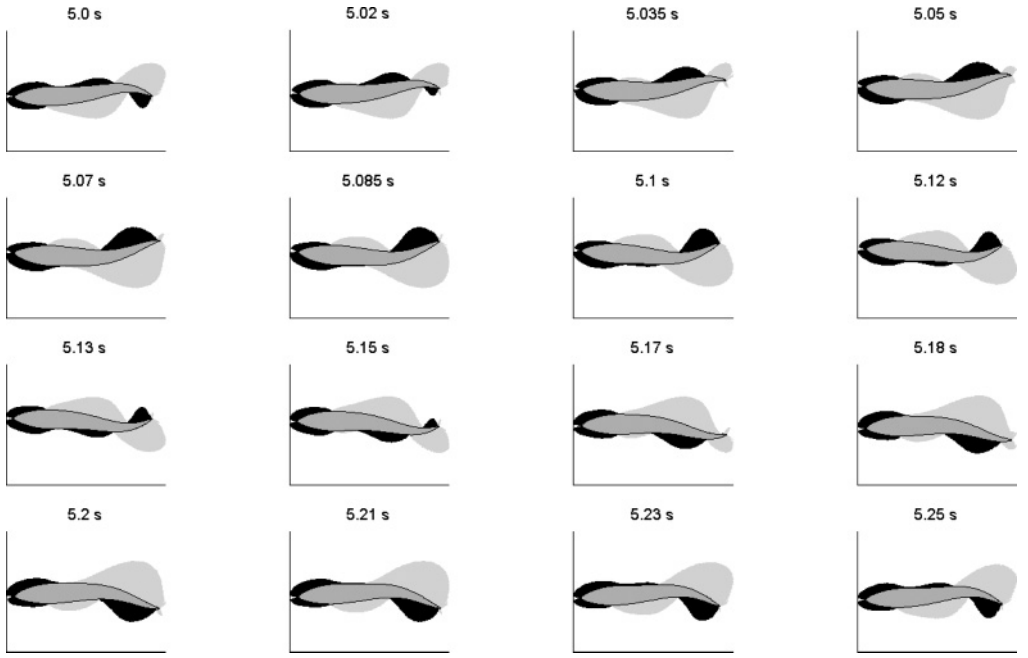

FIG. 14. Drag and thrust forces on the skin of the fish over time (in seconds, s), for tailbeat frequency of 3.8 Hz, unconstrained acceleration. Black indicates drag, gray thrust. Force areas are composed of lines perpendicular to the skin, with the length of the line indicating the relative size of the force on that segment of the skin.

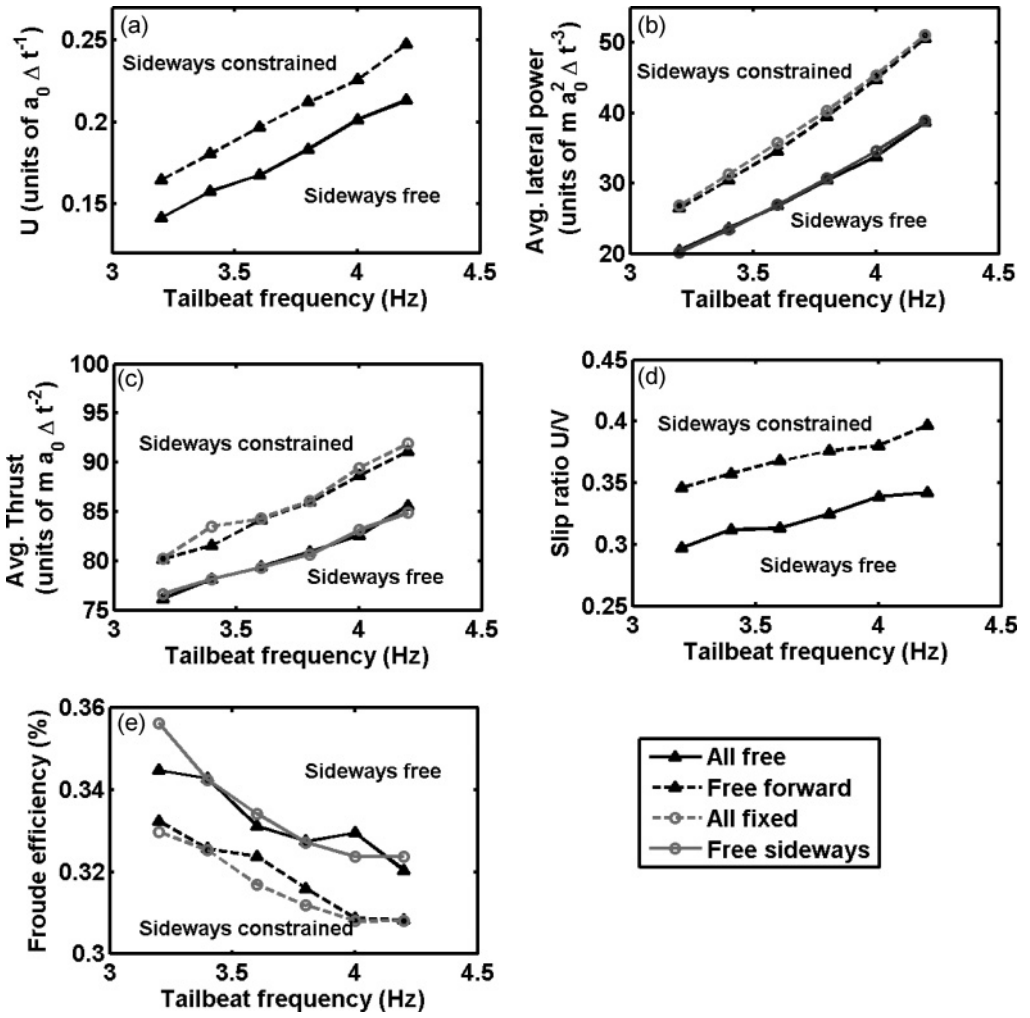

FIG. 15. Results of swimming fish that are either constrained or free in their forward and sideways acceleration, for several tailbeat frequencies. (a) Equilibrium forward swimming speed. (b) Average lateral power exerted (in simulation units) by the fish. (c) Average forward thrust component (in simulation units). (d) Slip ratio U/V. (e) Froude efficiency of the swimming fish Eq. (19).

with the swimming direction, implying that the wake widens [Figs. 16(a) and 16(b); see also Fig. 17]. The circulation in the wake increases significantly for the unconstrained fish [Fig. 16(c)]. For each of the sideways-constrained fish (twice $N = 6$, Spearman's $\rho = 0.77$ NS), and for the forward-only constrained fish (Spearman's $\rho = 0.83$ NS), however, tailbeat frequency does not significantly influence circulation strength. The Strouhal number is lower for higher tailbeat frequencies [Fig. 16(d)]. This implies that the vortices are closer to each other along the swimming direction.

Concerning the effects of constraint of sideways acceleration: Compared to no constraint, it significantly increases the swimming speed [Fig. 15(a)], sideways power [Fig. 15(b)], thrust [Fig. 15(c)], and the slip ratio U/V [Fig. 15(d)], and decreases the Froude efficiency [Fig. 15(e)]. For the wake, sideways constraint increases the size, angle, and circulation of the vortex rings [Figs. 16(a)–16(c) and 17] and decreases the Strouhal number [Fig. 16(d)]. Note that these results are all similar to those of an increased tailbeat frequency. This arises because the sideways constraint increases the sideways velocity of the tail of the fish throughout its tailbeat (Fig. 8), because the fish does not accelerate in the direction opposite to where its tail pushes the water.

The effect of forward constraint is hardly visible (Figs. 15 and 16), except for reducing the circulation if the fish is sideways free and increasing it if the fish is sideways constrained [Fig. 16(c)]. Since circulation is derived from the values of vorticity and vortex ring radius which are highly stochastic in our model, the importance of these differences is doubtful.

IV. DISCUSSION

The resemblance between the fluid dynamics in our model and empirical data of the physical model of a wing of a hovering insect [49] and of the undulating fish [21] shows the suitability of the multiparticle collision dynamics model for such studies.

Our results disagree with the two theoretical predictions (first, thrust exclusively produced by tailtip, and second, slip ratio as an estimator of efficiency) and further show problems with the use of constrained acceleration as a representation of

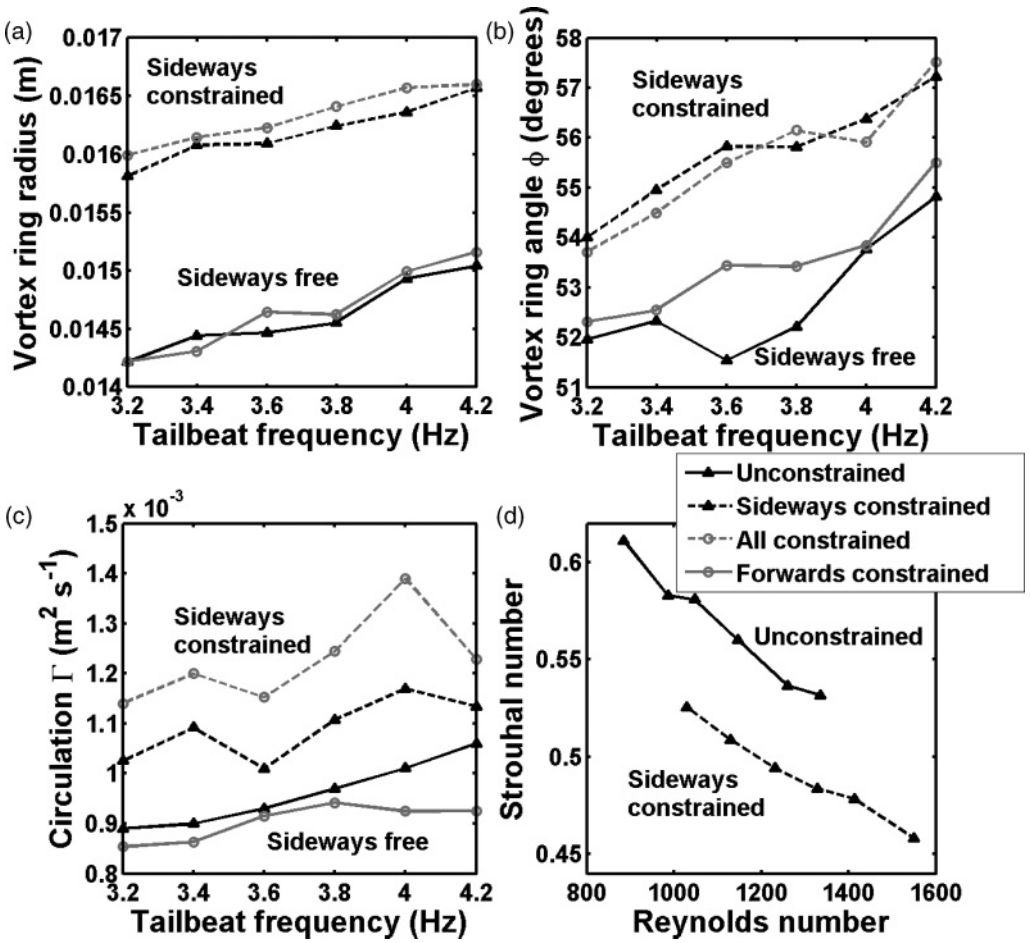

FIG. 16. Results of swimming fish that are either constrained or free in their forward and sideways acceleration, for several tailbeat frequencies. (a) Radius of the vortex rings in the wake of the fish. (b) Angle ϕ of the vortex rings with the forward swimming direction (Fig. 17). (c) Circulation Γ in the vortex rings of the wake. (d) Equilibrium Strouhal number of the swimming fish as a function of the Reynolds number.

natural swimming. As regards the first point, we show that the rear 2/3 of the body produces thrust at some point during the swimming cycle. Thus, empirical studies of the swimming of fish should investigate flow along the entire body rather than only focusing on the tailtip and the wake [21,23], as illustrated experimentally by Müller [61] and Anderson *et al.* [62].

As regards the second point, the slip ratio appears not to be an estimator of efficiency. The inverse relationship between

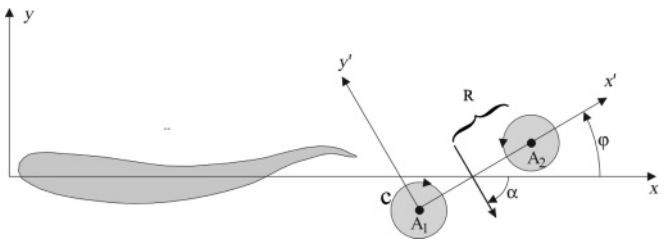

FIG. 17. Schematic overview of the wake structure of a mullet, after [21]. $A1$ and $A2$ are the centers of two adjacent vortices in the two-dimensional plane that comprise a vortex ring in a three-dimensional wake. R indicates the radius of the vortex ring, ϕ its angle relative to the swimming direction and α the angle relative to the swimming direction of the jet through the vortex ring.

it and Froude efficiency in our model is intriguing, because it is opposite of that predicted theoretically [11,31]. So far the relationship between slip ratio and efficiency has only been studied empirically for fish swimming behind pillars, where they appeared to be more efficient (in terms of lower muscle activity) and have a lower slip ratio [33]. However, this situation, where the flow was unsteady and undulation was largely passive, cannot really be compared to a fish that swims actively in uniform flow, and therefore more empirical data are needed to test our results. This should be done by measuring of a fish both kinematics and energy expenditure (for example by using respirometers as proposed by Liao [63]). In the meantime, our results warn against the common practice of using the slip ratio as an estimator of the efficiency of swimming fish [64,65].

Besides, our finding that the slip ratio U/V increases with the tailbeat frequency and Reynolds number is supported by our recent meta-analysis of empirical data [66].

Further, our results suggest that fish that are constrained not to accelerate sideways produce forces that qualitatively resemble those of unconstrained fish that have a higher tailbeat frequency. Simulation studies that constrain their fish sideways [14,15] are thus likely to overestimate all

the forces and accompanying kinematic and hydrodynamic patterns associated with a particular tailbeat frequency. The general relevance of this still needs to be tested in 3D models.

Three of our results are supported by those of other studies, both theoretical and empirical. First, Borazjani and Sotiropoulos [16] also found a reduction of Froude efficiency with an increase in Reynolds number in their simulations of a swimming eel. Second, the decrease of the Strouhal number with increasing Reynolds number in our model fits both computational results of a swimming mackerel by Borazjani and Sotiropoulos [15] and experimental data of swimming Pacific salmon of Lauder and Tytell [67]. Third, the increase in swimming speed with higher tailbeat frequency is consistent with empirical data of real fish [1,64]. As regards the consequences of tailbeat frequency for wake structure, our model serves as prediction.

Both in our study of an insect wing and of an undulating fish we compare a 2D model to a 3D experiment, yet we still find similar results. We suppose that in each case there are different reasons for the robustness against a reduction in dimension. For the insect wing, it may indicate that 3D effects, such as spanwise flow along the wing (which can be caused by the leading-edge vortex [68–70]) are not of great importance at low Reynolds numbers. Indeed, the artificial elimination of spanwise flow in a flapping model of a drosophila wing at a low Reynolds number (75) did not greatly influence the leading-edge vortex [68]. However, this robustness may not hold for higher Reynolds numbers, above 1400, because here a strong spanwise flow was found on the same wing [71]. In the case of the fish, the similarity of our results in a model in two dimensions to those of experiments in 3D may be a consequence of an increase in the effective Reynolds number due to the reduction in dimension. In two dimensions there is one fewer degree of freedom of movement and hence all phenomena—such as recirculation, vortex shedding, and turbulence—occur at less than half the Reynolds number than they do in 3D [18]. This may cause the similarity in Strouhal number of our results for a relatively low Reynolds number (1.2×10^3) to experimental data of a mullet by Müller *et al.* [21] at a much higher Reynolds number (30×10^3), and the resemblance of our mullet at Reynolds number 1150 to the three-dimensional carangiform model by Borazjani *et al.* [15] at a Reynolds number over 4000. The Froude efficiency in our model appears to be approximately 10% higher than in their 3D model. This may also be a consequence of the two-dimensionality: in 2D there is one fewer direction to waste power in. Further, we cannot exclude that details of results of our model such as the precise distribution of thrust along the body may be influenced by its two-dimensionality. For example, in reality the distribution of the force may be affected by the narrow caudal peduncle of a real fish, but this cannot be represented in a two-dimensional model where the fluid cannot flow over the top or bottom of the fish. However, despite such potential differences between 2D and 3D situations [72], we expect our results to apply qualitatively in three dimensions.

Our model has several weak points. First, mainly due to its high stochasticity, it is necessary to average over either large areas or long intervals to eliminate noise. For example spatial averaging is needed to obtain clear images of the vorticity around the undulating fish (Fig. 9). Second, the undulation of the fish was fixed and was not affected by the fluid forces. In future we intend to extend our model with a fish whose undulation is based on internal mechanics as well as being influenced by the surrounding fluid.

In sum, our results indicate the importance of several theoretical and empirical follow-up studies. For low-Reynolds simulations it may be possible to model organisms in a simpler manner, by linearizing the Navier-Stokes equations [73]. However, it remains to be tested whether this is also possible for unsteady motion such as the organisms in this study perform. Theoretically it would be of great interest to investigate in our model the swimming efficiency over a wider range of Reynolds numbers, body shapes, and swimming styles. It may also be of interest to test whether the extraordinary investment of fish larvae in an increase of their length and hence Reynolds number [74] comes at the cost of efficiency, or rather increases it. Empirically, the hypotheses concerning the effects of tailbeat frequency on various aspects of the kinematics and hydrodynamics of swimming are greatly in need of further study.

ACKNOWLEDGMENTS

We thank John Videler and James C. Liao as well as two anonymous referees for comments on an earlier version. H.H. was financed by Grant No. 012682-STARFLAG from the STREP program "Starflag" in the 6th European framework, awarded to C.K.H. J.T.P. thanks the Netherlands Organisation for Scientific Research (NWO) for financial support.

APPENDIX: RAY–MOVING LINE INTERSECTION

Let the ray be parametrically expressed in two dimensions as

$$\mathbf{r}(t) = \mathbf{r}_0 + t\, d\mathbf{r}. \tag{A1}$$

The particle is at $\mathbf{r}_0$ at the beginning of the current time step, which we identify with $t = 0$, and t is continuous time.

Let $\mathbf{p}(t)$ and $\mathbf{q}(t)$ similarly be the position of the end points of the moving line over time, as follows:

$$\mathbf{p}(t) = \mathbf{p}_0 + t\, d\mathbf{p}, \tag{A2}$$

$$\mathbf{q}(t) = \mathbf{q}_0 + t\, d\mathbf{q}. \tag{A3}$$

Any point on the edge can be expressed as $\mathbf{E}(s,t) = s\mathbf{q}(t) + (1-s)\mathbf{p}(t)$, where s is the coordinate along the edge. The movements of particle and edge intersect if at any time t' the equality $\mathbf{E}(s,t') = \mathbf{r}(t')$ holds; in other words

$$s(\mathbf{q}_0 + t'\, d\mathbf{q}) + (1-s)(\mathbf{p}_0 + t'\, d\mathbf{p}) = \mathbf{r}_0 + t'\, d\mathbf{r}. \tag{A4}$$

First we solve for t', focusing on the x component of Eq. (A4):

$$t' = -\frac{s(q_{0,x} - p_{0,x}) + (p_{0,x} - r_{0,x})}{s(dq_x - dp_x) + (dp_x - dr_x)}. \tag{A5}$$

Then we solve for t', focusing on the y component, with a result similar to the one above but with all subscripts x replaced by y. Equating the two expressions for t', we arrive at a quadratic equation in s:

$$as^2 + bs + c = 0, \tag{A6}$$

where the coeffients a, b, and c can be expressed using the binary perpendicular dot product ($\perp$), which greatly simplifies the coefficients of the quadratic equation and allows the solution to be calculated efficiently (note that $\perp$ is basically the z component of the cross product of vectors in the x-y plane):

$$\perp(\mathbf{A},\mathbf{B}) \equiv A_x B_y - A_y B_x, \tag{A7}$$

$$a = \perp(\mathbf{q}_0 - \mathbf{p}_0, d\mathbf{q} - d\mathbf{p}), \tag{A8}$$

$$b = \perp(\mathbf{q}_0 - \mathbf{p}_0, d\mathbf{p} - d\mathbf{r}) + \perp(\mathbf{p}_0 - \mathbf{r}_0, d\mathbf{q} - d\mathbf{p}), \tag{A9}$$

$$c = \perp(\mathbf{p}_0 - \mathbf{r}_0, d\mathbf{p} - d\mathbf{r}). \tag{A10}$$

Solving the quadratic equation yields two values for s, which, when inserted into Eq. (A5), give two corresponding values for t'. If any of the s lie in the interval $[0,1]$ and the corresponding t' lies in the interval $[0,\Delta t]$ a collision has occurred. If there are two solutions within this interval, the one with smallest t' occurred first and is picked for further processing.

[1] J. J. Videler, *Fish Swimming* (Chapman and Hall, London, 1993).
[2] M. V. Abrahams and P. W. Colgan, Environmental Biology of Fishes **13**, 195 (1985).
[3] J. Herskin and J. F. Steffensen, J. Fish Biol. **53**, 366 (1998).
[4] J. C. Svendsen, J. Skov, M. Bildsoe, and J. F. Steffensen, J. Fish Biol. **62**, 834 (2003).
[5] J. A. Walker, C. K. Ghalambor, O. L. Griset, D. McKenney, and D. N. Reznick, Functional Ecology **19**, 808 (2005).
[6] E. D. Tytell and G. V. Lauder, J. Exp. Biol. **211**, 3359 (2008).
[7] D. S. Barrett, M. S. Triantafyllou, D. K. P. Yue, M. A. Grosenbaugh, and M. J. Wolfgang, J. Fluid Mech. **392**, 183 (1999).
[8] P. R. Bandyopadhyay, Integr. Comp. Biol. **42**, 102 (2002).
[9] D. Weihs, Nature (London) **241**, 290 (1973).
[10] W. W. Schultz and P. W. Webb, Integr. Comp. Biol. **42**, 1018 (2002).
[11] J. Lighthill, J. Fluid Mech. **9**, 305 (1960).
[12] H. Liu, R. J. Wassersug, and K. Kawachi, J. Exp. Biol. **199**, 1245 (1996).
[13] M. J. Wolfgang, J. M. Anderson, M. A. Grosenbaugh, D. K. P. Yue, and M. S. Triantafyllou, J. Exp. Biol. **202**, 2303 (1999).
[14] Y. Sui, Y.-T. Chew, P. Roy, and H.-T. Low, Int. J. Numer. Methods Fluids **53**, 1727 (2007).
[15] I. Borazjani and F. Sotiropoulos, J. Exp. Biol. **211**, 1541 (2008).
[16] I. Borazjani and F. Sotiropoulos, J. Exp. Biol. **212**, 576 (2009).
[17] A. Malevanets and R. Kapral, Europhys. Lett. **44**, 552 (1998).
[18] D. A. P. Reid, H. Hildenbrandt, J. T. Padding, and C. K. Hemelrijk, Phys. Rev. E **79**, 046313 (2009).
[19] J. Gray, J. Exp. Biol. **10**, 88 (1933).
[20] E. J. Stamhuis and J. J. Videler, J. Exp. Biol. **198**, 283 (1995).
[21] U. K. Müller, B. L. E. van den Heuvel, E. J. Stamhuis, and J. J. Videler, J. Exp. Biol. **200**, 2893 (1997).
[22] U. K. Müller, E. J. Stamhuis, and J. J. Videler, J. Exp. Biol. **203**, 193 (2000).
[23] E. D. Tytell and G. V. Lauder, J. Exp. Biol. **207**, 1825 (2004).
[24] E. D. Tytell, J. Exp. Biol. **207**, 3265 (2004).
[25] J. O. Dabiri, J. Exp. Biol. **208**, 3519 (2005).
[26] G. Taylor, Proc. R. Soc. London A **214**, 158 (1952).
[27] T. Y. Wu, J. Fluid Mech. **10**, 321 (1961).
[28] J.-Y. Cheng, L.-X. Zhuang, and B.-G. Tong, J. Fluid Mech. **232**, 341 (1991).
[29] J. Carling, T. Williams, and G. Bowtell, J. Exp. Biol. **201**, 3143 (1998).
[30] T. McMillen and P. Holmes, J. Math. Biol. **53**, 843 (2006).
[31] M. J. Lighthill, Proc. R. Soc. London B **179**, 125 (1971).
[32] J. Cheng and R. Blickhan, J. Exp. Biol. **192**, 169 (1994).
[33] J. C. Liao, D. N. Beal, G. V. Lauder, and M. S. Triantafyllou, J. Exp. Biol. **206**, 1059 (2003).
[34] A. Gilmanov and F. Sotiropoulos, J. Comput. Phys. **207**, 457 (2005).
[35] I. Borazjani, L. Ge, and F. Sotiropoulos, J. Comput. Phys. **227**, 7587 (2008).
[36] R. Mittal, IEEE J. Oceanic Eng. **29**, 595 (2004).
[37] C. S. Peskin, Acta Numerica **11**, 479 (2002).
[38] J. J. Monaghan, Annu. Rev. Astron. Astrophys. **30**, 543 (1992).
[39] J. Kajtar and J. Monaghan, J. Comput. Phys. **227**, 8568 (2008).
[40] A. Malevanets and R. Kapral, J. Chem. Phys. **110**, 8605 (1999).
[41] N. Kikuchi, C. M. Pooley, J. F. Ryder, and J. Yeomans, J. Chem. Phys. **119**, 6388 (2003).
[42] J. T. Padding and A. A. Louis, Phys. Rev. E **74**, 031402 (2006).
[43] Y. Yang, J. Elgeti, and G. Gompper, Phys. Rev. E **78**, 061903 (2008).
[44] M. Ripoll, R. G. Winkler, and G. Gompper, Phys. Rev. Lett. **96**, 188302 (2006).
[45] H. Noguchi and G. Gompper, Proc. Natl. Acad. Sci. USA **102**, 14159 (2005).
[46] M. J. Lighthill, *Mathematical Biofluiddynamics* (SIAM, 1975).
[47] G. S. Triantafyllou, M. S. Triantafyllou, and M. A. Grosenbaugh, J. Fluids Struct. **7**, 205 (1993).
[48] T. J. Pedley and S. J. Hill, J. Exp. Biol. **202**, 3431 (1999).
[49] Z. J. Wang, J. M. Birch, and M. H. Dickinson, J. Exp. Biol. **207**, 449 (2004).
[50] T. Ihle and D. M. Kroll, Phys. Rev. E **63**, 020201 (2001).
[51] A. Lamura, G. Gompper, T. Ihle, and D. M. Kroll, Europhys. Lett. **56**, 319 (2001).
[52] Y. Inoue, Y. Chen, and H. Ohashi, Comput. Phys. Commun. **142**, 114 (2001).
[53] M. H. Dickinson, F.-O. Lehmann, and S. P. Sane, Science **284**, 1954 (1999).
[54] J. J. Videler and F. Hess, J. Exp. Biol. **109**, 209 (1984).
[55] S. Vogel, *Life in Moving Fluids* (Princeton University Press, 1996).
[56] A. Lamura and G. Gompper, Eur. Phys. J. E **9**, 477 (2002).
[57] S. P. Sane and M. H. Dickinson, J. Exp. Biol. **205**, 1087 (2002).
[58] MathWorks, MATLAB, r2006a.
[59] M. Sun and J. Tang, J. Exp. Biol. **205**, 2413 (2002).
[60] See Supplemental Material at http://link.aps.org/supplemental/10.1103/PhysRevE.85.021901 for a video of the swimming fish shape.
[61] U. K. Müller, J. Smit, E. J. Stamhuis, and J. J. Videler, J. Exp. Biol. **204**, 2751 (2001).

[62] E. J. Anderson, W. R. McGillis, and M. A. Grosenbaugh, J. Exp. Biol. **204**, 81 (2001).
[63] J. C. Liao, Philos. Trans. R. Soc. London B **362**, 1973 (2007).
[64] G. B. Gillis, J. Exp. Biol. **201**, 949 (1998).
[65] U. K. Müller, E. J. Stamhuis, and J. J. Videler, Integr. Comp. Biol. **42**, 981 (2002).
[66] F. van Weerden, D. A. P. Reid, and C. K. Hemelrijk (unpublished).
[67] G. V. Lauder and E. D. Tytell, Fish Physiology **23**, 425 (2006).
[68] J. M. Birch and M. H. Dickinson, Nature (London) **412**, 729 (2001).
[69] D. Lentink, W. B. Dickinson, J. L. v. Leeuwen, and M. H. Dickinson, Science **324**, 1438 (2009).
[70] E. J. Stamhuis, J. J. Videler, L. A. van Duren, and U. K. Müller, Exp. Fluids **33**, 801 (2002).
[71] J. M. Birch, W. B. Dickson, and M. H. Dickinson, J. Exp. Biol. **207**, 1063 (2004).
[72] S. Kern and P. Koumoutsakos, J. Exp. Biol. **209**, 4841 (2006).
[73] M. Roper and M. P. Brenner, Proc. Natl. Acad. Sci. USA **106**, 2977 (2009).
[74] U. K. Müller and J. J. Videler, Reviews in Fish Biology and Fisheries **6**, 353 (1996).